

The curvature of spectral energy distribution of blazars

Liang Chen^{1,2}

ABSTRACT

The broadband spectral energy distribution (SED) of blazars show significant curvature. In this paper, we study the curvature properties for a large sample of *Fermi*/LAT bright blazars based on quasi-simultaneous SED. Both SEDs of synchrotron and inverse Compton (IC) components are fitted by a log-parabolic law in $\log \nu$ - $\log \nu f_\nu$ diagram. The second-degree term of log-parabola measures the curvature of SED. We find a statistically significant correlation between synchrotron peak frequency and its curvature. This result is in agreement with the theoretical prediction, and confirms previous studies, which dealt with single source with various epoch observations or a small sample. If a broken power-law is employed to fit the SED (spectral indexes α_1 and α_2 , before and after the peak frequency, respectively), the difference between the two spectral indexes (i.e., $|\alpha_2 - \alpha_1|$) can be considered as a “surrogate” of the SED curvature. We collect spectral parameters of a sample blazars from literature, and find a correlation between the synchrotron peak frequency and the spectral difference. We do not find a significant correlation between the IC peak frequency and its curvature, which may be caused by complicated seed photon field. It is also found that the synchrotron curvatures are on average larger than that of IC curvatures, and there is no correlation between these two parameters. As suggested by previous works in literature, both the log-parabolic law of SED and above correlation can be explained by statistical and/or stochastic particle accelerations. Stochastic particle acceleration predicts a different slope of the correlation from that of statistical one, and our result seems favor stochastic acceleration mechanisms and emission processes. Some of other evidences also seem to support that the electron energy distribution (and/or synchrotron SED) may be log-parabolic, which include

¹Key Laboratory for Research in Galaxies and Cosmology, Shanghai Astronomical Observatory, Chinese Academy of Sciences, 80 Nandan Road, Shanghai 200030, China; chenliang@shao.ac.cn

²Key Laboratory of Modern Astronomy and Astrophysics (Nanjing University) Ministry of Education, Nanjing 210093, China

SED modeling, particle acceleration simulation, and comparisons between some predictions and empirical relations/correlations.

Subject headings: galaxies: active - BL Lacertae objects: general - galaxies: jets - radiation mechanisms: non-thermal

1. Introduction

As early as 1970s, people noted that the non-thermal spectra of blazar show significant curvature. Rieke & Kinman (1974) found the infrared (IR) spectrum is significantly flatter than that of optical for OJ 287. Many other blazars, like BL Lacertae, 0735+178, ON 231, B2 0912+29, B2 1215+30, and AO 0253+164 also present similar properties (Rieke & Kinman 1974; Odell et al. 1977; Sitko et al. 1983). Ghisellini et al. (1986) claimed that there is apparent difference between slopes of IR and ultraviolet (UV), with a mean value of $\Delta\alpha = 0.49 \pm 0.14$ (see also, Brown et al. 1989). Blazar SED shows more clear curvature and some present significant breaks, when combine broadband emissions (radio through X-ray bands, Ledden et al. 1981; Ledden & Odell 1985; Brodie et al. 1987). Further researches revealed a component on blazar SED from radio to UV/X-ray bands in $\log \nu$ - $\log \nu f_\nu$ diagram, which is widely interpreted as synchrotron emissions of high energy electrons in a relativistic jet closely aligned to our line of sight (see e.g., Blandford & Rees 1978; Landau et al. 1986; Urry & Padovani 1995; Sambruna et al. 1996; Ghisellini et al. 1989, 1998). Some high energy detectors have broad energy coverage, e.g, *BeppoSAX* covering 0.1-300 keV (LECS: 0.1-10 keV, MECS: 1.3-10 keV, and PDS: 13-300 keV). And hence, with observations of some of the telescopes alone, blazar SEDs are found to be curved, some of which can be fitted by a log-parabolic law. For instance, X-ray observations of Mrk 501 and Mrk 421 (see, Massaro et al. 2004a,b, 2008, and references and citations therein), together with several other BL Lacs (PKS 0548-322, 1H 1426+418, 1ES 1959+650, and PKS 2155-304; see, Massaro et al. 2008) show that X-ray spectra can be fitted by log-parabolic law, i.e., $\log \nu f_\nu = -b(\log \nu - \log \nu_p)^2 + \log \nu_p f_{\nu_p}$. Massaro et al. (2011a) studied a sample of high-frequency-peaked BL Lac objects (HBLs), and found that X-ray spectral curvature (measured by the second-term b) of TeV HBLs are systematically larger than that of those HBLs non-detected at TeV energies (NBL), implying that the NBL X-ray spectra are systematically narrower (see also, Massaro et al. 2013).

For the first time, BL Lac object Mrk 421 was detected by Whipple emitting γ -ray photons at TeV band (Punch et al. 1992). Thanks to development of many ground based Cherenkov telescopes (e.g., Whipple, MAGIC, VERITAS, H.E.S.S., CANGAROO), more than 50 blazars have now been discovered bearing TeV γ -ray emissions (see, <http://tevcat.uchicago.edu>).

At GeV γ -ray band, *CGRO*/EGRET successfully detected 68 AGNs with significance $\sigma > 5$ (working at 20 MeV - 30 GeV, most of them are blazars, Hartman et al. 1999). As a successor, *Fermi*/LAT works between 20 MeV - 300 GeV, which was launched at June 2008. During the first 11 months survey of *Fermi*/LAT, 671 AGNs were detected with high confidence level at high Galactic latitude ($|b| > 10^\circ$, $\sigma > 5$, and most of them are blazars, see Abdo et al. 2010c). The number increases to 1017, through first two years survey of *Fermi*/LAT (Ackermann et al. 2011). Based on these γ -ray observations, another component on blazar SED was discovered, peaking at γ -ray band. These γ -ray emissions are usually explained as inverse Compton emissions (IC) of the same electron population accounting for the synchrotron component emissions (see, Ghisellini et al. 1998, 2010; Abdo et al. 2010b, and references therein). Many blazars observed by *Fermi*/LAT alone present curved γ -ray spectra and some can be well fitted by a log-parabolic law (see, e.g., Ackermann et al. 2011). Higher energy observation of some blazars (e.g., PKS 2155-304, Mrk 501, Mrk 421, see, Aharonian et al. 2007; Ghisellini & Tavecchio 2008; Samuelson et al. 1998; Krennrich et al. 1999; Aleksić et al. 2012) by Imaging Atmospheric Cherenkov Telescopes (IACT) show substantial curvature at TeV band, and some can also be fitted by log-parabolic law. If combine the GeV data with those of TeV, the spectra present more significant curvature (see, Abdo et al. 2009c; Zhang et al. 2012; Şentürk et al. 2013).

To characterize a broadband peaked component, one needs at least two parameters: peak frequency and peak flux/luminosity. These two parameters are extensively used in blazar studies, especially in the so called blazar sequence (see e.g., Fossati et al. 1998; Ghisellini et al. 1998; Chen & Bai 2011; Giommi et al. 2012). If log-parabolic law is adopted to fit the peaked component, i.e., $\log \nu f_\nu = -b(\log \nu - \log \nu_p)^2 + \log \nu_p f_{\nu_p}$, the second-term b measures the curvature around the SED peak, which is the third important parameter to characterize the component. Using multi-epoch observations of Swift, XMM-Newton, and *BeppoSAX*, it was found that each observational X-ray spectra of Mrk 421 can be well fitted by a log-parabolic law, and an anti-correlation between the peak frequency ν_p and the curvature b is discovered (see, Massaro et al. 2004a; Tramacere et al. 2007, 2009). Further, Massaro et al. (2008) extend the study to several other BL Lacs, e.g., Mrk 501, PKS 2155-304, PKS 0548-322, and found that all these BL Lacs present similar behavior: an anti-correlation between the peak frequency ν_p and the curvature b . As expected by previous theoretical investigations, the anti-correlation between peak frequency and curvature can be explained in the framework of acceleration processes of emitting electrons (see, Tramacere et al. 2007; Paggi et al. 2009b,a, and the Section 2 in this work). More detailed study on this third parameter, the curvature, is necessary to understand the particle acceleration, and energy dissipation mechanism in blazars.

Besides the high energy study, low energy observations from radio to optical also il-

lustrate a similar feature. For example, Landau et al. (1986) fitted the SED from radio to optical with a log-parabolic law of a sample of 18 blazars. Except for 3 bad fitted or steep radio spectral blazars, they found an anti-correlation between peak frequency and curvature for the remaining 15 blazars (see the top panel of Fig. 3 in Landau et al. 1986). In the past nearly three decades, many large samples of blazars were used to study the properties of the peak frequency, luminosity, and jet emission parameters (see, Sambruna et al. 1996; Fossati et al. 1998; Ghisellini et al. 1998; Nieppola et al. 2006; Chen et al. 2009; Wu et al. 2009; Ghisellini et al. 2010; Abdo et al. 2010b; Chen & Bai 2011). However, few works focused on the curvature properties by using broadband SEDs. Until recently, Rani et al. (2011) presented an anti-correlation between synchrotron peak frequency and curvature by fitting the SEDs from radio to optical of 10 BL Lacs in both high and low states.

In this paper, we collect quasi-simultaneous broadband SEDs, from radio to γ -ray, of a large sample of blazars. Both SEDs of synchrotron and IC components are fitted by log-parabolic law in $\log \nu$ - $\log \nu f_\nu$ diagram, respectively, and we obtain the synchrotron and IC curvatures. We then present detailed studies on the correlations between the peak frequency and curvature, and implications of the results. This paper is organized as follows: Section 2 shows the theoretical interpretation of the correlation between the peak frequency and curvature. Section 3 describes the sample, and Section 4 shows the fitting procedures. After providing the results in Section 5, the detailed discussions and implications of the results are presented in Section 6. We end with a summary of the findings in Section 7. Throughout the paper, a Λ CDM cosmology with values within 1σ of the *Wilkinson Microwave Anisotropy Probe* (*WMAP*) results (Komatsu et al. 2011) is used; in particular, $H_0 = 70 \text{ km s}^{-1} \text{ Mpc}^{-1}$, $\Omega_\Lambda = 0.73$, and $\Omega_M = 0.27$.

2. Theory of the Correlation

Two different scenarios can explain the correlation between peak frequency and curvature, i.e., statistical and the stochastic acceleration mechanisms, both of which can reproduce the electron energy distribution as a log-parabolic law. A log-parabolic distribution of electron energy also emits a log-parabolic SED approximately, which consists with the fitting methods (see, Massaro et al. 2004a,b, 2006; Tramacere et al. 2007; Massaro et al. 2008; Tramacere et al. 2011, and references therein). In the following, we will explain the difference between these two acceleration mechanisms, that will be tested with our results in this work.

The first scenario is in the framework of statistical acceleration, which needs either an energy-dependent acceleration probability (p_a) or a fluctuation of fractional acceleration gain

(ε). For the case of energy-dependent acceleration probability, Massaro et al. (2004a) showed that when acceleration efficiency is inversely proportional to the energy itself ($p_a = g/\gamma^q$ and $\varepsilon = \text{cons.}$ in this case), the log-parabolic law would be a very good approximation of the electron energy distribution,

$$N(\gamma) \approx \text{cons.} \left(\frac{\gamma}{\gamma_0} \right)^{-s-r \log(\gamma/\gamma_0)}. \quad (1)$$

Where γ_0 is initial electron energy, $r = q/(2 \log \varepsilon)$ is curvature of electron energy distribution, and $s = -2r/q \log(g/\gamma_0) - (q - 2)/2$. The SED of synchrotron emissions by these electrons is also approximately log-parabolic, i.e., $\log \nu L_\nu = -b_{sy} (\log \nu - \log \nu_p)^2 + \log \nu_p L_{\nu_p}$. With monochromatic emission assumption (i.e., δ -approximation), one can derive the synchrotron peak frequency $\nu_p \propto \gamma_p^2$ and curvature $b_{sy} = r/4$, where $\log \gamma_p = \log \gamma_0 + (3 - s)/2r$ is the peak energy of electron in diagram $\log \gamma - \log \gamma^3 N(\gamma)$. As suggested by Massaro et al. (2006), one obtains $b_{sy} \approx r/5$ instead of $b_{sy} = r/4$, when release the assumption of δ -approximation. After substituting the γ_p , s and r , we obtain $\log \nu_p = C + 2 \log \gamma_0 + (3 - s)/r = C + 2 \log \gamma_0 + 2/q \log(g/\gamma_0) + \log \varepsilon + 2/r$. Assuming that γ_0 , q , g , and ε are independent variables and substituting the relation $b_{sy} \approx r/5$, we get $\log \nu_p \approx C_1 + 2/(5b_{sy})$. For the case of fluctuations of fractional acceleration gain, Tramacere et al. (2011) showed that when ε is a random variable around a systematic energy gain $\bar{\varepsilon}$ ($p_a = 1$ and $\varepsilon = \bar{\varepsilon} + \chi$ in this case, where random variable χ has a probability density function with zero mean value and variance σ_ε^2), applying the multiplicative case of the central limit theorem, one derives the electron energy distribution at acceleration step n_s ,

$$N(\gamma) = \frac{N_0}{\gamma \sigma_\gamma \sqrt{2\pi}} \exp \left[-\frac{(\ln \gamma - \mu)^2}{2\sigma_\gamma^2} \right]. \quad (2)$$

Where $\sigma_\gamma^2 \approx n_s (\sigma_\varepsilon / \bar{\varepsilon})^2$ and $\mu = \ln \gamma_0 + n_s [\ln \bar{\varepsilon} - (\sigma_\varepsilon / \bar{\varepsilon})^2 / 2]$. Therefore, the electron peak energy and curvature in diagram $\log \gamma - \log \gamma^3 N(\gamma)$ can be derived: $\log \gamma_p = \log \gamma_0 + n_s \log \bar{\varepsilon} + 3/(4r)$ and $r = \ln 10 / [2n_s (\sigma_\varepsilon / \bar{\varepsilon})^2]$. Substituting the relation $b_{sy} \approx r/5$ and γ_b , we have $\log \nu_p \approx C + 2 \log \gamma_0 + 2n_s \log \bar{\varepsilon} + 3/(10b)$. Assuming that γ_0 , n_s , $\bar{\varepsilon}$ and σ_ε are independent variables, we obtain $\log \nu_p \approx C + 3/(10b_{sy})$.

The second scenario is in the framework of stochastic acceleration, provided the Fokker-Planck equation with presence of a momentum-diffusion term. Kardashev (1962) suggested that a log-parabolic distribution of electron energy can be derived from a ‘quasi-monoenergetic particle injection (i.e., $N_{\text{inj}}(\gamma) \approx N_0 \delta(\gamma - \gamma_0)$, see also Tramacere et al. 2007, 2011),

$$N(\gamma) = \frac{N_0}{\gamma \sqrt{4\pi a_1}} \exp \left[-\frac{(\ln \gamma - a_1 - a_2 - \ln \gamma_0)^2}{4a_1} \right]. \quad (3)$$

Where a_1 and a_2 correspond stochastic and systematic acceleration terms, respectively. When represented in diagram $\log \gamma$ - $\log \gamma^3 N(\gamma)$, we obtain the curvature $r = \ln 10/4a_1$, and the electron peak energy $\log \gamma_p = \log \gamma_0 + 5a_1/\ln 10 + a_2/\ln 10 = \log \gamma_0 + a_2/\ln 10 + 5/(4r)$. Assuming that γ_0 , a_1 and a_2 are independent variables and substituting the relation $b_{sy} \approx r/5$ and γ_p , we have $\log \nu_p \approx C + 1/(2b_{sy})$.

3. The Sample

Abdo et al. (2010b) collected broadband quasi-simultaneous spectral data, from radio through γ -ray, of 48 LBAS (*Fermi* LAT Bright AGN Sample, see Abdo et al. 2009a) blazars based on the first three months operation of *Fermi*/LAT. All these data are properly scaled in $\log \nu$ - $\log \nu f_\nu$ diagram. The 48 LBAS blazars are taken as our sample in this paper, and the detailed information of these blazars are presented in Table 1. Column (1) provides the *Fermi*/LAT name of the source. Column (2) is the source redshift. The broadband spectral data of these blazars are also taken from Abdo et al. (2010b). Figure 6 in the Appendix are the SED of these 48 blazars. The red points are the broadband quasi-simultaneous spectral data, while the grey ones represent other observations (see, Abdo et al. 2010b, for detail description).

4. The Fitting Procedure

In order to get the curvatures of synchrotron and IC components, we adopt a log-parabolic law, i.e., $\log \nu f_\nu = -b(\log \nu - \log \nu_p)^2 + \log \nu_p f_{\nu_p}$, to fit the quasi-simultaneous SED of the two components, respectively (same as in Landau et al. 1986; Sambruna et al. 1996; Massaro et al. 2004a,b; Nieppola et al. 2006; Wu et al. 2009; Massaro et al. 2008; Rani et al. 2011; Massaro et al. 2011a). The coefficient of the second degree term, b_{sy}/b_{IC} , measures the curvature around the peak. The least χ^2 technique is used to determine the parameters. For some blazars, there are no quasi-simultaneous data (the red points in the Figure 6) at radio or microwave bands to constrain the lower energy part of synchrotron fitting. We add other observation data (i.e., the grey points) in the fitting. For some data points, the errors are unavailable. We estimate the errors with average errors of those data points whose errors are available. Since the errors of the data for the synchrotron component are usually much smaller than that for the IC component, we derive the average errors of the data in the two components separately. The best fitting parameter values are listed in Table 1. Columns (3), (4), (5), (6), and (7) are the (for synchrotron fitting) peak frequency, flux, curvature, the degree of freedom, and the reduced χ^2 , respectively. Columns (8), (9), (10), (11), and

(12) denote the same quantities but for IC fitting.

In order to test the validity of our fitting parameters, we compare the peak fluxes and peak frequencies between ours and those obtained from Abdo et al. (2010b) by fitting a third degree polynomial function for both SEDs of synchrotron and IC components, respectively. The comparison results are shown in Figure 1. The top left panel is for synchrotron peak frequency comparison, top right for synchrotron peak flux comparison, bottom left for IC peak frequency comparison, and bottom right for IC peak flux comparison. The red lines are the best linear fits. The Pearson test shows that they are all tightly correlated, with Pearson’s probability for a null correlation negligible ($p = 1.14 \times 10^{-24}$, 3.81×10^{-19} , 2.24×10^{-18} , and 4.23×10^{-18} for synchrotron peak frequency comparison, synchrotron peak flux comparison, IC peak frequency comparison, and IC peak flux comparison, respectively). Therefore, our log-parabolic fittings present similar parameter values as that of Abdo et al. (2010b).

The synchrotron fitting curves of total 48 blazars are plotted as red solid lines in Figure 6 in Appendix. We check all the fitted SEDs (one by one) by naked eyes. From these Figures, it can be seen that the X-ray emissions of 14 blazars belong to the synchrotron components (see Figure 6 and Table 1 for the name list). The IC components of these blazars cover only γ -ray band, and therefore the IC fitted parameters may be unreliable because of the narrow SED coverage. These 14 IC fitted curves are plotted as red dashed lines in the Figure 6. For blazars J0238.6+1636, J0538.8-4403, J2254.0+1609, and J2345.5-1559, it can be seen that the fitted spectra at *Fermi* γ -ray band are much harder than the observed spectra. These 4 IC fitted curves are plotted as red dotted lines. For blazars J1719.3+1746 and 2202.4+4217, there are no observational data at the right wing of IC component, and therefore the fitted curvatures (b_{IC}) may be unreliable. In fact, the value of b_{IC} of these two blazars are significantly smaller than that of others (see Table 1). These two IC fitted curves are also plotted as red dashed lines. Because of above reasons, we exclude these 20 (= 14 + 4 + 2) blazars in the following analysis concerning the IC component. The IC fitted curves of remaining 28 blazars are presented as red solid lines. Among these 48 blazars, 43 sources have measured redshifts (see Table 1). The peak luminosities and frequencies (in AGN frame) can be calculated through $(\nu_p L_{\nu_p})_{s,C} = 4\pi d_L^2 (\nu_p f_{\nu_p})_{s,C}$ and $(\nu_p)_{s,C} = (1+z)(\nu_p)_{s,C}^{obs}$, where d_L is the luminosity distance and z is the source redshift. In the following analysis, all values (e.g., peak frequency and curvature) are indicated in AGN frame, noticing that the curvature b is unchanged when transform from observational to AGN frames.

5. The Results

From Table 1, we can see that the value of synchrotron curvature b_{sy} varies between 0.056 and 0.27. The range of the value is larger than that of any previous studies (see, Landau et al. 1986; Massaro et al. 2004a,b, 2008; Rani et al. 2011; Massaro et al. 2011a). We plot the synchrotron curvature versus peak frequency in Figure 2. Here we use $1/b_{sy}$ instead of b_{sy} to represent the synchrotron curvature, since it will be convenient to compare with the theoretical results (see Section 2). The black squares denote these 43 blazars having measured redshift. The Pearson test presents a small p -value, $p = 1.35 \times 10^{-17}$. The red solid line is the best linear fitting, which gives $1/b_{sy} = -(22.08 \pm 0.43) + (2.04 \pm 0.03) \log \nu_p^{sy}$ and the dashed red lines indicate the 1σ confidence bands. Hence, the synchrotron peak frequency correlates with its curvature at a high level of confidence.

Among these 28 blazars whose IC curvatures are well estimated, 26 blazars have measured redshift. Similar to the synchrotron one, we plot the IC peak frequency versus IC curvature in Figure 3. The black squares denote these 26 blazars. The Pearson test shows a very weak correlation, with p -value $p = 5.16 \times 10^{-2}$, which is mainly contributed by the object J1504.4+1030 (the red point in the Figure 3, through jackknife statistical test¹).

6. Discussion and Conclusions

Blazars are observationally subdivided into flat spectrum radio quasars (FSRQs) and BL Lacertae objects (BL Lacs), based on presence or absence of emission lines (see, Scarpa & Falomo 1997). Our sample includes 48 blazars, in which 43 sources have measured redshift. The sample is not large enough to separate them into various subclasses, e.g., FSRQs versus BL Lacs. FSRQs and BL Lacs show continuous properties, although they are divided by some criterions (e.g., the equivalent width of emission line $\geq 5 \text{ \AA}$, the Eddington ratio $\dot{m} \sim 0.01$, see Scarpa & Falomo 1997; Ghisellini et al. 2009; Xu et al. 2009, and references therein). Nowadays when discuss *Fermi*/LAT detected blazars, the terms Low Synchrotron Peaked blazars (LSP), Intermediate Synchrotron Peaked blazars (ISP) and High Synchrotron Peaked blazars (HSP) are often used instead of FSRQs and BL Lacs (see, e.g., Abdo et al. 2010b,c).

Because of possible importance of the correlation between the synchrotron peak frequency and curvature (see Section 2), many works have studied the correlation (Massaro et al. 2004a; Tramacere et al. 2007, 2009; Massaro et al. 2008; Landau et al. 1986; Rani et al.

¹We estimate the p -value for each subsample by omitting the i th object. And it is found that the p -value reaches maximum, $p = 0.118$, when omitting the object J1504.4+1030.

2011). These works are based on either the X-ray data of single sources or small samples using data from radio to optical. In this paper, we study the correlation using a sample of 48 blazars, whose broadband quasi-simultaneous SEDs are from radio to γ -ray. The correlation between the synchrotron peak frequency and curvature depicted in this work confirm the results of these previous works.

As an alternative to log-parabolic fitting, a broken power-law of electron energy distribution is commonly used to fit the SED in both synchrotron self-Compton (SSC) and external Compton (EC) models (see e.g., Tavecchio et al. 1998; Böttcher & Dermer 2002; Georganopoulos & Kazanas 2003; Ghisellini et al. 2005; Bai 2005; Abdo et al. 2009b, 2010a; Chen et al. 2012, and references therein). Therefore, if the above correlation between the peak frequency and curvature is genuine, there should be a similar correlation even a broken power-law is employed to fit SED. From electron energy distribution to blazar SED, the spectral indexes transform as $\alpha_{1,2} = (p_{1,2} - 1)/2$ approximately, where p_1 and p_2 are electron energy indexes below and above the break. In this case, the difference between the spectral indexes (i.e., $|\alpha_2 - \alpha_1| = |p_2 - p_1|/2$) can be considered as a “surrogate” of the curvature (b_{sy}), and one expects a correlation between synchrotron peak frequency and this “curvature”. We collect the data of 24 blazars (at both high and low states) from Zhang et al. (2012) to test the correlation, which are plotted in Figure 4 (similar to $1/b_{sy}$, here we use $1/|\alpha_2 - \alpha_1|$). The visual inspection shows a positive correlation between these two quantities, if excluding two obviously departure points (marked as green triangle and blue star). The green triangle represents high state of Mrk 501. From the Fig. 1 of Zhang et al. (2012), it can be seen that there are no spectral data above the synchrotron peak to constrain the spectral index (α_2/p_2), and the index adopted by the authors is significantly larger than that at lower state ($p_2^{\text{high}} = 4.6$ versus $p_2^{\text{low}} = 3.72$, see Table 1 of Zhang et al. 2012). The blue star represents the high state of PKS 2005-489, whose SED fitting is not very good: the value of synchrotron peak may be underestimated and the value of spectral index below the synchrotron peak may be overestimated (see the Fig. 1 of Zhang et al. 2012). For these reasons, we exclude these two points. The Pearson’s test yields a significant correlation with $p = 5.35 \times 10^{-5}$. Therefore, even a broken power-law is employed to fit SED, there is also a correlation between the “curvature” and the synchrotron peak frequency. Although there are different mathematic functions to describe blazar SED (log-parabolic law versus broken power-law), these two correlations represent an identical property of blazar SED.

Based on SSC model, Paggi et al. (2009a) predicted a relation between curvatures of IC and synchrotron components, $b_{\text{SSC}} \approx b_{\text{sy}}/2$ at Thomson regime, while $b_{\text{SSC}} \approx 5b_{\text{sy}}$ at Klein-Nishina (KN) regime (see also, Paggi et al. 2009b). The SSC peak frequency is $\nu_p^{\text{SSC}} \propto \nu_p \gamma_p^2 \propto \gamma_p^4$ for Thomson scattering, and $\nu_p^{\text{SSC}} \propto \gamma_p$ for KN scattering, respectively. As discussed in Section 2 (see also, Tramacere et al. 2007; Paggi et al. 2009b,a), the peak

energy of electron (γ_p) correlates with the synchrotron curvature (b_{sy}). We therefore expect a correlation between SSC peak frequency and curvature at Thomson or KN regimes. For the first time, we study the relation between the IC peak frequency and curvature from observational view, while our results present no significant correlation with a chance probability only $p = 0.0516$. This is due to the following reasons:

- The IC component is sometimes a composite of SSC and EC emissions.
- The IC emission may lie at Thomson regime for some blazars, while others are at KN regime.
- The intrinsic spectrum of a single IC scattering is broader than the intrinsic synchrotron spectrum of a single electron (see, Figures 6.6 versus 7.3 in Rybicki & Lightman 1979), and the SED of seed photons are usually very broad.

These reasons will significantly broaden the SED of IC component, and the value of IC curvature is more uncertain relative to the synchrotron one. We note that these reasons lead to another two predictions. Firstly, the synchrotron curvature (b_{sy}) would be on average larger than that of IC component (b_{IC}) at Thomson regime. Secondly, there would be very weak or no correlation between the two curvatures. These two predictions are confirmed by Figure 5, which shows IC curvature versus synchrotron curvature (represented by $1/b_{IC}$ versus $1/b_{sy}$), and the red solid line shows a perfect one-to-one relation.

As suggested in Section 2, two scenarios can explain the observed correlation between synchrotron peak frequency and curvature. Theoretical predictions of the slope B (in $1/b_{sy} = A + B \log \nu_p$) are $B = 5/2$, $10/3$, and 2 for models of energy-dependent acceleration probability, fluctuation of fractional acceleration gain, and stochastic acceleration, respectively. Our observational result $B = 2.04 \pm 0.03$ (see Section 5) is consistent with the stochastic acceleration mechanisms and emission processes.

Some of other evidences seem to support that the electron energy distribution may be log-parabolic. Taking the synchrotron radiation and a three-dimensional turbulent electromagnetic field configuration into account, Nodes et al. (2004) presented numerical simulations of particle acceleration. They found, in a few cases, energy spectral index characterized by a steepening spectra at high energies. Massaro et al. (2006) verified that these spectra can be represented well by a log-parabolic law or by a combination of a power law and a parabola. Cerruti et al. (2013) presented a detailed SED modeling of 3C 454.3 and finds that its GeV γ -ray break could be well reproduced if electron energy distribution is log-parabolic. In order to fit the SED of MeV blazars, Sikora et al. (2002) assumed that electrons are accelerated via a two-step process with a broken power-law energy distribution as injection. Taking

the cooling effect into account, Massaro et al. (2006) verified that these resulting electron spectra can be well described by a log-parabola over a range wider than three decades. The log-parabolic law of synchrotron component of SED are also found to be consistent with some empirical relations/correlations (see Appendix for detail).

7. Summary

The curvature, in addition to peak frequency and peak flux, is the third important parameter to characterize a broadband SED, which may shine out the hidden electron energy distribution, particle acceleration mechanism, energy dissipation mechanism, and many other blazar properties. A larger sample of blazars with high quality SED is needed to check these results in detail, especially for the IC components. We summarize the main results of this paper as follows.

- We found a significant correlation between the curvature (in $1/b_{sy}$) and peak frequency for synchrotron component and no significant correlation between same quantities for IC component. It is also found that the synchrotron curvatures are on average larger than that of IC curvatures, and there is no correlation between the two parameters. This may be caused by complicated seed photon field.
- The difference between spectral indexes above and below the SED peak of 24 blazars (at both high and low states) are calculated (i.e., $|\alpha_2 - \alpha_1|$, data from Zhang et al. 2012). We found a significant correlation between $1/|\alpha_2 - \alpha_1|$ and the synchrotron peak frequency. Parameter $|\alpha_2 - \alpha_1|$ can be considered as a “surrogate” of the curvature. Therefore, this result confirms the correlation between the synchrotron peak frequency and curvature, even provided a broken power-law fit of SED.
- We found that the slop of correlation between synchrotron curvature of peak frequency ($B = 2.04 \pm 0.03$) is consistent with the prediction of stochastic scenario.
- Some of other evidences also seem to support that the electron energy distribution (and/or synchrotron SED) may be log-parabolic, which include SED modeling, particle acceleration simulation, and comparisons between some predictions and empirical relations/correlations.

We thank the anonymous referee for insightful comments and constructive suggestions. We are grateful to the help from Xinwu Cao, Jinming Bai, Jin Zhang and Wentao Luo.

This work is supported by the NSFC (grants 11233006, 11133006, 11173043, 11103054 and 11103060), and XTP project XDA04060604.

REFERENCES

- Abdo, A. A., Ackermann, M., Ajello, M., et al. 2009a, *ApJ*, 700, 597
- Abdo, A. A., Ackermann, M., Ajello, M., et al. 2009b, *ApJ*, 699, 31
- Abdo, A. A., Ackermann, M., Ajello, M., et al. 2009c, *ApJ*, 707, 1310
- Abdo, A. A., Ackermann, M., Agudo, I., et al. 2010a, *ApJ*, 721, 1425
- Abdo, A. A., Ackermann, M., Agudo, I., et al. 2010b, *ApJ*, 716, 30
- Abdo, A. A., Ackermann, M., Ajello, M., et al. 2010c, *ApJ*, 715, 429
- Ackermann, M., Ajello, M., Allafort, A., et al. 2011, *ApJ*, 743, 171
- Aharonian, F., Akhperjanian, A. G., Bazer-Bachi, A. R., et al. 2007, *ApJ*, 664, L71
- Aleksić, J., Alvarez, E. A., Antonelli, L. A., et al. 2012, *A&A*, 542, A100
- Böttcher, M., & Dermer, C. D. 2002, *ApJ*, 564, 86
- Bai, J.-M. 2005, *Chinese Journal of Astronomy and Astrophysics Supplement*, 5, 207
- Blandford, R. D., & Rees, M. J. 1978, *BL Lac Objects*, 328
- Brodie, J., Bowyer, S., & Tennant, A. 1987, *ApJ*, 318, 175
- Brown, L. M. J., Robson, E. I., Gear, W. K., et al. 1989, *ApJ*, 340, 129
- Cerruti, M., Dermer, C. D., Lott, B., Boisson, C., & Zech, A. 2013, *ApJ*, 771, L4
- Chen, L., & Bai, J. M. 2011, *ApJ*, 735, 108
- Chen, L., Cao, X., & Bai, J. M. 2012, *ApJ*, 748, 119
- Chen, Z., Gu, M., & Cao, X. 2009, *MNRAS*, 397, 1713
- Fossati, G., Maraschi, L., Celotti, A., Comastri, A., & Ghisellini, G. 1998, *MNRAS*, 299, 433
- Georganopoulos, M., & Kazanas, D. 2003, *ApJ*, 594, L27
- Ghisellini, G., Celotti, A., Fossati, G., Maraschi, L., & Comastri, A. 1998, *MNRAS*, 301, 451
- Ghisellini, G., Maraschi, L., & Tavecchio, F. 2009, *MNRAS*, 396, L105

- Ghisellini, G., Maraschi, L., Treves, A., & Tanzi, E. G. 1986, *ApJ*, 310, 317
- Ghisellini, G., & Tavecchio, F. 2008, *MNRAS*, 386, L28
- Ghisellini, G., Tavecchio, F., & Chiaberge, M. 2005, *A&A*, 432, 401
- Ghisellini, G., Tavecchio, F., Foschini, L., et al. 2010, *MNRAS*, 402, 497
- Ghisellini, G., George, I. M., & Done, C. 1989, *MNRAS*, 241, 43P
- Giommi, P., Padovani, P., Polenta, G., et al. 2012, *MNRAS*, 420, 2899
- Hartman, R. C., Bertsch, D. L., Bloom, S. D., et al. 1999, *ApJS*, 123, 79
- Kardashev, N. S. 1962, *Soviet Ast.*, 6, 317
- Komatsu, E., Smith, K. M., Dunkley, J., et al. 2011, *ApJS*, 192, 18
- Krennrich, F., Biller, S. D., Bond, I. H., et al. 1999, *ApJ*, 511, 149
- Landau, R., Golisch, B., Jones, T. J., et al. 1986, *ApJ*, 308, 78
- Ledden, J. E., & Odell, S. L. 1985, *ApJ*, 298, 630
- Ledden, J. E., Odell, S. L., Stein, W. A., & Wisniewski, W. Z. 1981, *ApJ*, 243, 47
- Massaro, E., Perri, M., Giommi, P., & Nesci, R. 2004a, *A&A*, 413, 489
- Massaro, E., Perri, M., Giommi, P., Nesci, R., & Verrecchia, F. 2004b, *A&A*, 422, 103
- Massaro, E., Tramacere, A., Perri, M., Giommi, P., & Tosti, G. 2006, *A&A*, 448, 861
- Massaro, F., Paggi, A., Elvis, M., & Cavaliere, A. 2011a, *ApJ*, 739, 73
- Massaro, F., Tramacere, A., Cavaliere, A., Perri, M., & Giommi, P. 2008, *A&A*, 478, 395
- Massaro, F., Paggi, A., Errando, M., et al. 2013, *ApJS*, 207, 16
- Nieppola, E., Tornikoski, M., & Valtaoja, E. 2006, *A&A*, 445, 441
- Nodes, C., Birk, G. T., Gritschneider, M., & Lesch, H. 2004, *A&A*, 423, 13
- Odell, S. L., Puschell, J. J., Stein, W. A., & Warner, J. W. 1977, *ApJ*, 214, L105
- Padovani, P., & Giommi, P. 1995, *ApJ*, 444, 567
- Padovani, P., Perlman, E. S., Landt, H., Giommi, P., & Perri, M. 2003, *ApJ*, 588, 128

- Paggi, A., Massaro, F., Vittorini, V., et al. 2009a, *A&A*, 504, 821
- Paggi, A., Cavaliere, A., Vittorini, V., & Tavani, M. 2009b, *A&A*, 508, L31
- Punch, M., Akerlof, C. W., Cawley, M. F., et al. 1992, *Nature*, 358, 477
- Rani, B., Gupta, A. C., Bachev, R., et al. 2011, *MNRAS*, 417, 1881
- Rieke, G. H., & Kinman, T. D. 1974, *ApJ*, 192, L115
- Rybicki, G. B., & Lightman, A. P. 1979, New York, Wiley-Interscience, 1979. 393 p.,
- Sambruna, R. M., Maraschi, L., & Urry, C. M. 1996, *ApJ*, 463, 444
- Samuelson, F. W., Biller, S. D., Bond, I. H., et al. 1998, *ApJ*, 501, L17
- Scarpa, R., & Falomo, R. 1997, *A&A*, 325, 109
- Şentürk, G. D., Errando, M., Böttcher, M., & Mukherjee, R. 2013, *ApJ*, 764, 119
- Sikora, M., Błażejowski, M., Moderski, R., & Madejski, G. M. 2002, *ApJ*, 577, 78
- Sitko, M. L., Stein, W. A., Zhang, Y.-X., & Wisniewski, W. Z. 1983, *PASP*, 95, 724
- Tavecchio, F., Maraschi, L., & Ghisellini, G. 1998, *ApJ*, 509, 608
- Tramacere, A., Giommi, P., Massaro, E., et al. 2007, *A&A*, 467, 501
- Tramacere, A., Giommi, P., Perri, M., Verrecchia, F., & Tosti, G. 2009, *A&A*, 501, 879
- Tramacere, A., Massaro, E., & Taylor, A. M. 2011, *ApJ*, 739, 66
- Tramacere, A., Massaro, F., & Cavaliere, A. 2007, *A&A*, 466, 521
- Urry, C. M., & Padovani, P. 1995, *PASP*, 107, 803
- Wu, Z.-Z., Gu, M.-F., & Jiang, D.-R. 2009, *Research in Astronomy and Astrophysics*, 9, 168
- Xu, Y.-D., Cao, X., & Wu, Q. 2009, *ApJ*, 694, L107
- Zhang, J., Liang, E.-W., Zhang, S.-N., & Bai, J. M. 2012, *ApJ*, 752, 157

Table 1. The SED Fitting Parameters

Name(OFGL)	redshift	ν_p^{sy}	$(\nu f_\nu)_p^{sy}$	b_{sy}	dof _{sy}	$\chi^2_{sy,r}$	ν_p^{IC}	$(\nu f_\nu)_p^{IC}$	b_{IC}	dof _{IC}	$\chi^2_{IC,r}$
(1)	(2)	(3)	(4)	(5)	(6)	(7)	(8)	(9)	(10)	(11)	(12)
J0033.6-1921*	0.610	15.607±0.066	-11.160±0.029	0.106±0.003	11	0.4145	24.265±0.335*	-10.955±0.120*	0.480±0.297*	1	0.7803
J0050.5-0928*	—	14.626±0.059	-10.842±0.063	0.101±0.005	11	2.6429	22.962±0.448*	-10.578±0.043*	0.178±0.169*	1	0.0001
J0137.1+4751	0.859	13.347±0.078	-10.502±0.083	0.176±0.014	8	0.6019	22.304±0.330	-10.550±0.075	0.069±0.012	7	1.7003
J0210.8-5100	1.003	13.156±0.019	-10.965±0.017	0.149±0.003	35	17.7985	22.467±0.219	-10.232±0.035	0.074±0.008	11	4.8359
J0222.6+4302*	0.444	14.714±0.025	-10.400±0.018	0.117±0.002	40	2.6078	23.682±0.038*	-10.147±0.028*	0.237±0.013*	13	4.3426
J0229.5-3640	2.115	13.446±0.290	-11.928±0.206	0.146±0.033	7	0.8482	21.745±0.126	-10.332±0.069	0.126±0.011	8	2.1163
J0238.4+2855	1.213	12.765±0.037	-11.285±0.043	0.156±0.006	12	1.1031	22.058±0.382	-10.737±0.097	0.074±0.017	5	1.9191
J0238.6+1636†	0.940	12.973±0.021	-10.421±0.026	0.227±0.005	47	10.7721	24.604±1.085†	-9.899±0.074†	0.031±0.009†	16	34.6859
J0349.8-2102	2.944	13.087±0.032	-11.055±0.111	0.214±0.015	8	0.4579	21.891±0.119	-10.205±0.061	0.172±0.015	2	0.4180
J0423.1-0112	0.915	13.017±0.023	-10.893±0.028	0.168±0.006	35	1.0149	21.317±0.130	-10.368±0.096	0.099±0.013	7	2.6917
J0428.7-3755	1.112	13.582±0.073	-11.211±0.030	0.130±0.005	20	2.7216	22.986±0.177	-10.223±0.024	0.070±0.005	12	6.1359
J0449.7-4348*	0.205	15.105±0.032	-10.375±0.020	0.111±0.002	24	9.9664	24.025±0.895*	-10.531±0.045*	0.037±0.011*	4	1.2272
J0457.1-2325	1.003	13.104±0.062	-10.992±0.068	0.167±0.009	10	1.1554	22.507±0.156	-10.091±0.058	0.091±0.007	10	5.7873
J0507.9+6739*	0.416	17.186±0.568	-10.783±0.078	0.071±0.011	17	0.0690	25.738±0.735*	-10.607±0.144*	0.088±0.054*	5	2.1029
J0516.2-6200	—	13.550±0.177	-11.515±0.107	0.141±0.017	14	0.4809	22.612±0.298	-10.726±0.024	0.067±0.008	20	4.6043
J0531.0+1331	2.070	12.640±0.015	-11.295±0.021	0.174±0.004	39	7.5104	21.422±0.079	-9.953±0.066	0.145±0.011	10	4.8000
J0538.8-4403†	0.892	13.062±0.033	-10.400±0.042	0.191±0.006	18	1.8883	24.520±0.919†	-10.164±0.053†	0.032±0.008†	17	1.2905
J0712.9+5034	—	13.557±0.647	-11.213±0.477	0.155±0.101	3	0.0340	23.365±1.375	-11.000±0.069	0.052±0.025	4	0.7682
J0722.0+7120*	0.310	14.620±0.021	-9.978±0.016	0.130±0.002	62	5.8716	23.003±0.353*	-10.380±0.025*	0.046±0.007*	3	1.2265
J0730.4-1142	1.589	12.876±0.076	-10.572±0.226	0.200±0.033	6	17.0701	22.333±0.128	-10.104±0.036	0.095±0.007	10	6.9697
J0855.4+2009	0.306	13.429±0.014	-10.148±0.011	0.210±0.003	38	16.4465	21.346±0.161	-10.482±0.086	0.075±0.012	13	1.2470
J0921.2+4437	2.190	13.016±0.051	-10.926±0.082	0.205±0.014	5	2.2666	22.077±0.334	-10.734±0.064	0.058±0.011	9	1.8761
J1015.2+4927*	0.212	16.183±0.097	-10.580±0.024	0.078±0.003	17	3.3939	24.676±0.280*	-10.610±0.071*	0.067±0.025*	4	2.0654
J1058.9+5629	0.143	15.057±0.063	-10.884±0.040	0.103±0.003	11	1.8680	21.551±0.118	-10.692±0.059	0.103±0.016	18	2.3297
J1057.8+0138	0.888	12.961±0.160	-10.813±0.302	0.186±0.045	5	0.1860	21.896±0.462	-10.819±0.136	0.062±0.019	5	0.9898
J1104.5+3811*	0.030	16.689±0.056	-9.299±0.021	0.089±0.002	47	25.3150	24.249±0.057*	-10.066±0.033*	0.147±0.011*	13	3.1334
J1159.2+2912	0.729	12.942±0.023	-10.712±0.027	0.219±0.004	16	6.4871	22.501±0.418	-10.737±0.059	0.059±0.011	11	2.7382
J1221.7+2814*	0.102	14.927±0.034	-10.675±0.023	0.113±0.002	33	11.1198	24.312±0.089*	-10.458±0.057*	0.156±0.031*	15	4.6653
J1229.1+0202	0.158	14.134±0.172	-9.990±0.034	0.089±0.007	18	1.9384	20.802±0.035	-9.579±0.023	0.081±0.003	26	2.1859
J1248.7+5811*	—	14.590±0.043	-10.946±0.038	0.136±0.004	10	1.0594	22.885±1.426*	-10.969±0.094*	0.117±0.285*	1	0.2037
J1256.1-0548	0.536	12.760±0.008	-10.247±0.019	0.206±0.003	30	13.6854	22.073±0.179	-10.208±0.099	0.076±0.018	12	0.7205
J1310.6+3220	0.997	12.966±0.025	-10.659±0.051	0.239±0.008	10	2.4370	22.764±0.263	-10.442±0.023	0.060±0.007	14	3.5332
J1457.6-3538	1.424	13.688±0.095	-11.256±0.044	0.128±0.008	9	5.0165	22.344±0.256	-10.095±0.080	0.084±0.012	6	2.3088
J1504.4+1030	1.839	13.191±0.049	-10.863±0.069	0.185±0.012	11	0.9404	23.624±0.318	-9.895±0.032	0.063±0.007	12	5.2857
J1512.7-0905	0.360	13.271±0.024	-11.095±0.013	0.132±0.003	30	17.7053	22.193±0.170	-9.999±0.061	0.088±0.009	14	2.6933
J1522.2+3143	1.487	12.925±0.065	-12.078±0.124	0.144±0.019	10	4.7695	22.192±0.176	-10.172±0.097	0.132±0.014	3	2.8494
J1543.1+6130*	—	14.404±0.042	-11.292±0.048	0.137±0.004	13	5.0679	24.819±3.734*	-11.082±0.287*	0.035±0.032*	2	0.0362
J1653.9+3946*	0.033	16.551±0.083	-10.317±0.026	0.061±0.002	44	0.7394	25.033±0.220*	-10.674±0.110*	0.097±0.041*	6	0.1482
J1719.3+1746*	0.137	13.585±0.098	-11.453±0.057	0.138±0.010	10	0.5019	24.493±0.387*	-10.644±0.033*	0.036±0.004*	10	2.7840
J1751.5+0935	0.322	12.871±0.079	-10.207±0.224	0.270±0.034	5	0.6216	22.036±0.215	-10.324±0.083	0.088±0.013	6	0.4860
J1849.4+6706	0.657	13.753±0.039	-10.938±0.021	0.141±0.003	14	45.2431	22.573±0.313	-10.443±0.055	0.065±0.010	8	0.9814
J2000.2+6506*	0.047	17.886±0.171	-10.154±0.023	0.056±0.002	29	2.0107	24.492±0.103*	-10.629±0.078*	0.177±0.045*	6	2.3534
J2143.2+1741	0.213	14.192±0.036	-10.661±0.074	0.146±0.006	8	3.1776	21.829±0.296	-10.531±0.127	0.091±0.021	3	0.1145
J2158.8-3014*	0.116	15.479±0.032	-9.874±0.018	0.116±0.002	40	6.1386	23.789±0.057*	-10.167±0.026*	0.203±0.013*	11	1.8782
J2202.4+4217*	0.069	14.295±0.042	-10.185±0.009	0.129±0.003	40	9.5177	21.848±0.331*	-10.723±0.055*	0.034±0.009*	23	1.4534
J2254.0+1609†	0.859	12.791±0.013	-9.966±0.015	0.233±0.003	33	23.2350	22.698±0.155†	-9.674±0.028†	0.048±0.004†	22	6.1458
J2327.3+0947	1.843	12.965±0.025	-11.191±0.031	0.190±0.005	7	10.4132	21.587±0.082	-10.289±0.045	0.119±0.008	15	1.6895
J2345.5-1559†	0.621	13.666±0.148	-11.803±0.068	0.117±0.013	7	2.6984	22.993±0.536†	-10.717±0.029†	0.069±0.014†	5	9.0312

Note. — Column (1) provides the LAT name of the source. Column (2) is the source redshift. Columns (3), (4), (5), (6), and (7) are the (for the synchrotron fitting) peak frequency, flux, curvature, the degree of freedom, and the reduced χ^2 , respectively. Columns (8), (9), (10), (11), and (12) denote the same quantities but for IC fitting. The primes ‘*’ represent 14 blazars whose IC components cover only γ -ray band, and J1719.3+1746 and J2202.4+4217 whose fitting values of curvature b_{IC} are obviously smaller than that of other blazars. The IC fitting curves of these 16 blazars are shown as red dashed lines in Figure 6 in Appendix. The prime ‘†’ represent 4 blazars whose IC fitting curve significantly departure from the observational SED, especially inconsistent with the γ -ray spectral index. The IC fitting curves of these 4 blazars are presented as red dotted lines. See context for detail.

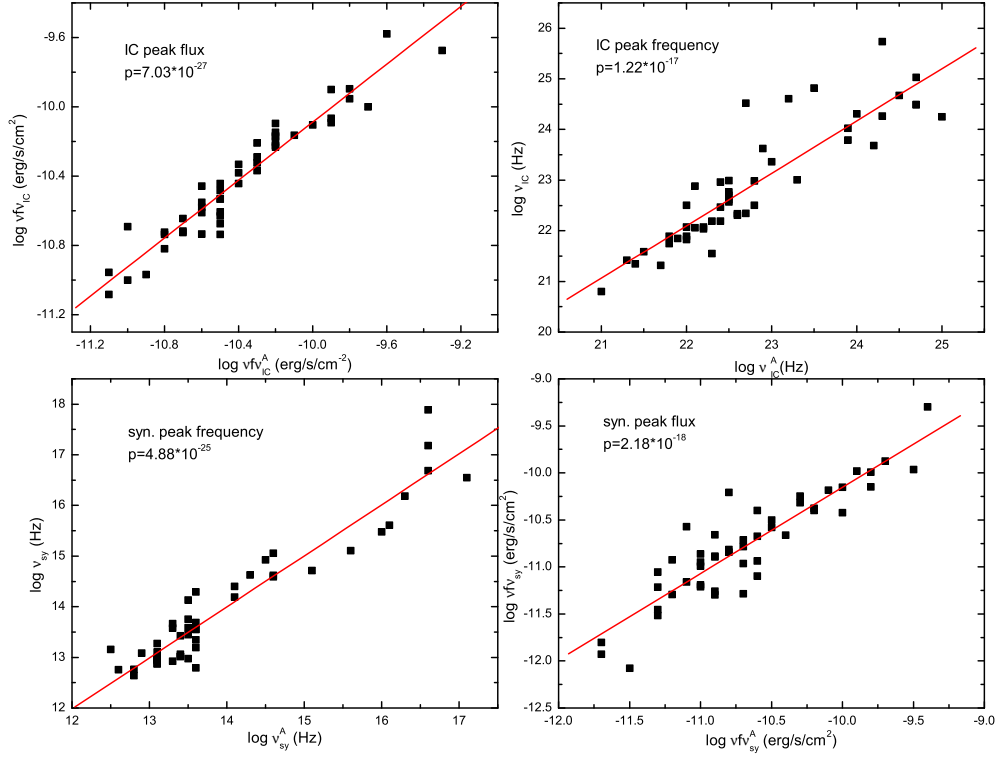


Fig. 1.— The comparisons between our fitting results and Abdo et al. (2010b) results. The top left panel is for synchrotron peak frequency comparison, top right panel for synchrotron peak flux comparison, bottom left panel for IC peak frequency comparison, and the bottom right panel for IC peak flux comparison. The red lines are for best linear fittings. The p -value in each panel is the Pearson’s probability for a null correlation.

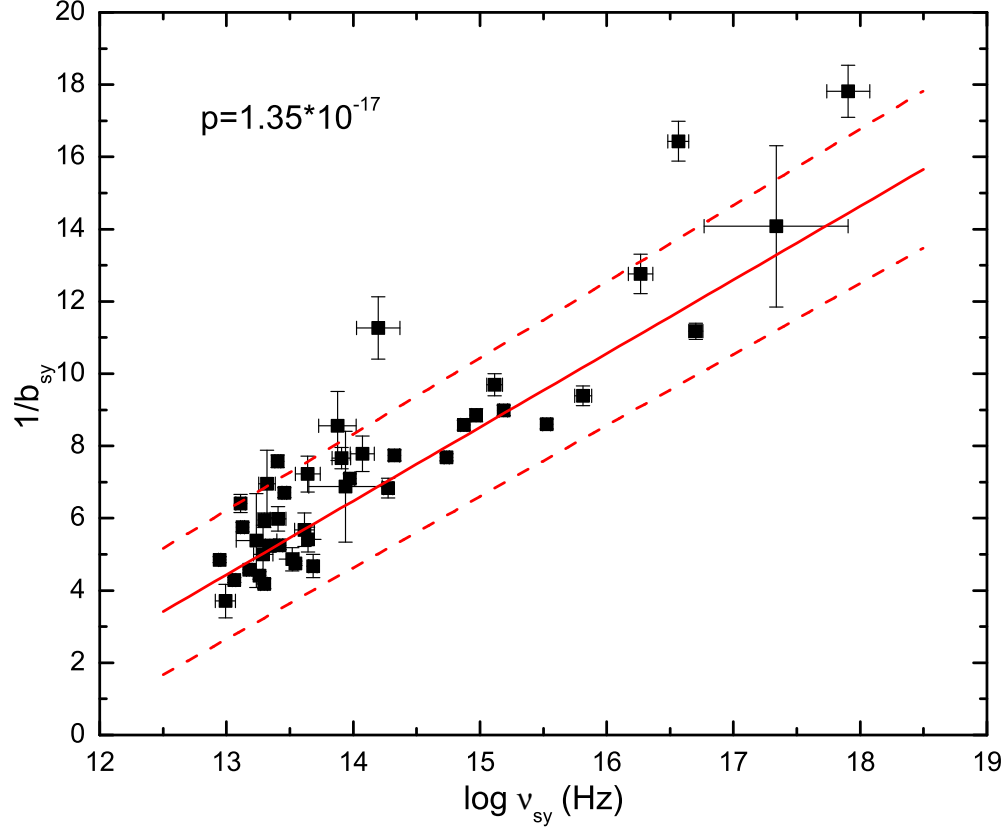


Fig. 2.— The synchrotron peak frequency versus curvature (in $1/b_{sy}$). The squares denote the total 43 sources with measured redshift. The Pearson test shows a significant correlation with a p -value, $p = 1.35 \times 10^{-17}$. The red solid line is the best linear fitting, which gives $1/b_{sy} = -(22.08 \pm 0.43) + (2.04 \pm 0.03) \log \nu_p^{sy}$ and the dashed red lines indicate 1σ confidence bands.

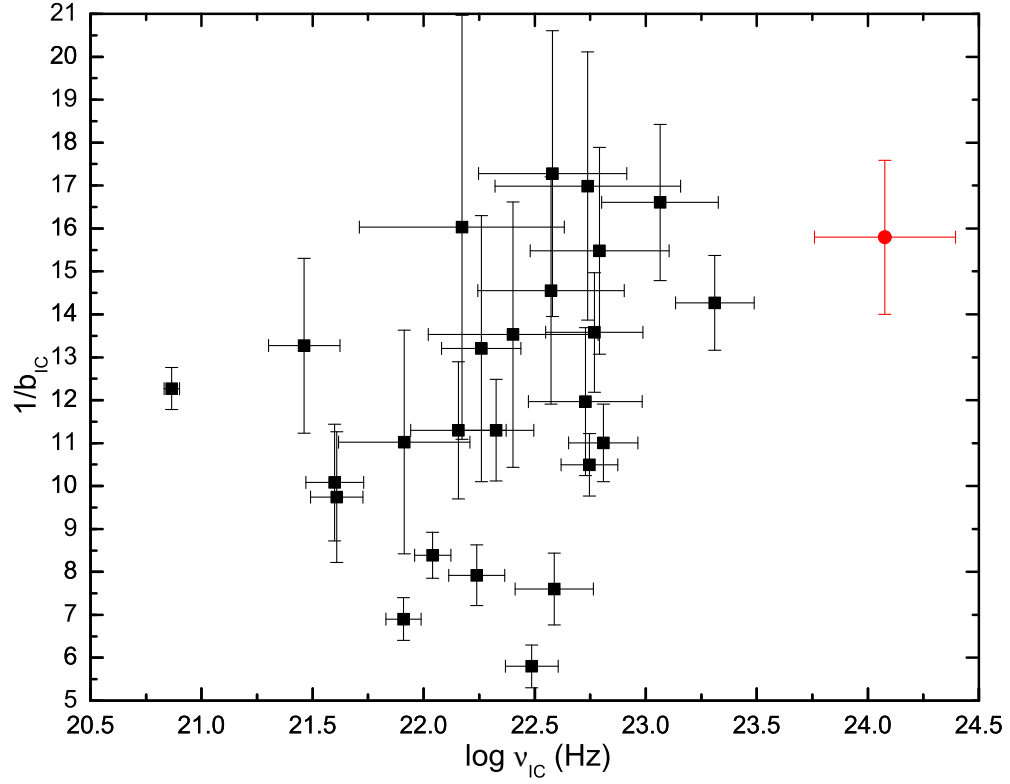


Fig. 3.— The IC peak frequency versus curvature (in $1/b_{IC}$). The black squares denote the total 26 blazars having measured redshift and reliable curvature estimated. The Pearson test shows a very weak correlation, with a p -value $p = 5.16 \times 10^{-2}$, which is mainly contributed by the object J1504.4+1030 (the red point).

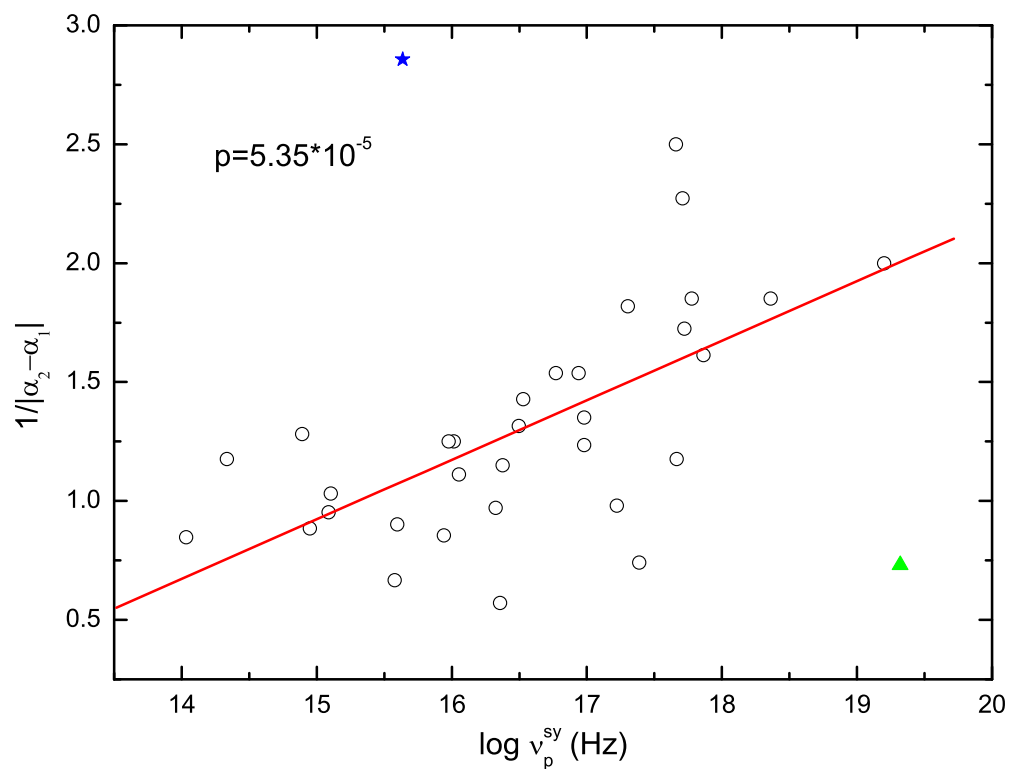


Fig. 4.— Synchrotron peak frequency versus the difference between spectral indexes above and below the peak (in $1/|\alpha_2 - \alpha_1|$). Data are taken from Zhang et al. (2012). The blue star and green triangle represent high states of PKS 2005-489 and Mrk 501. We exclude these two data points because of possibly unreliable values of parameter (see context for detail). The Pearson test presents a significant correlation with $p = 5.35 \times 10^{-5}$.

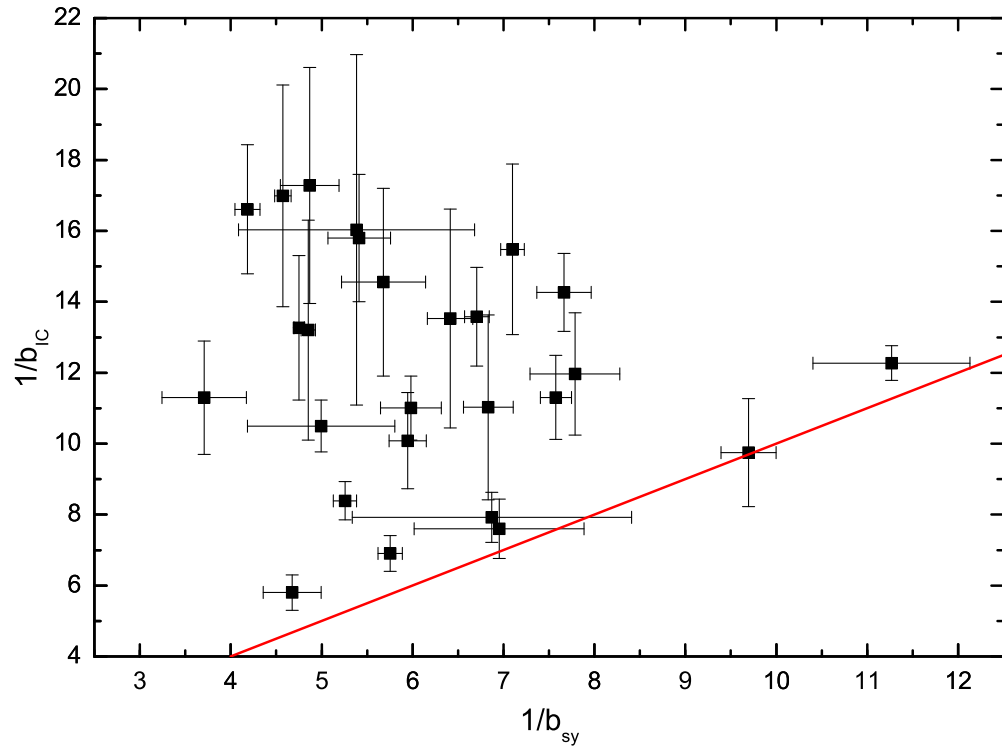


Fig. 5.— The synchrotron curvature versus the IC curvature. The red solid line shows a perfect one-to-one relation. It can be seen that the synchrotron curvature (b_{sy}) is on average larger than that of IC component (b_{IC}), and there is no correlation between these two parameters. See context for detail.

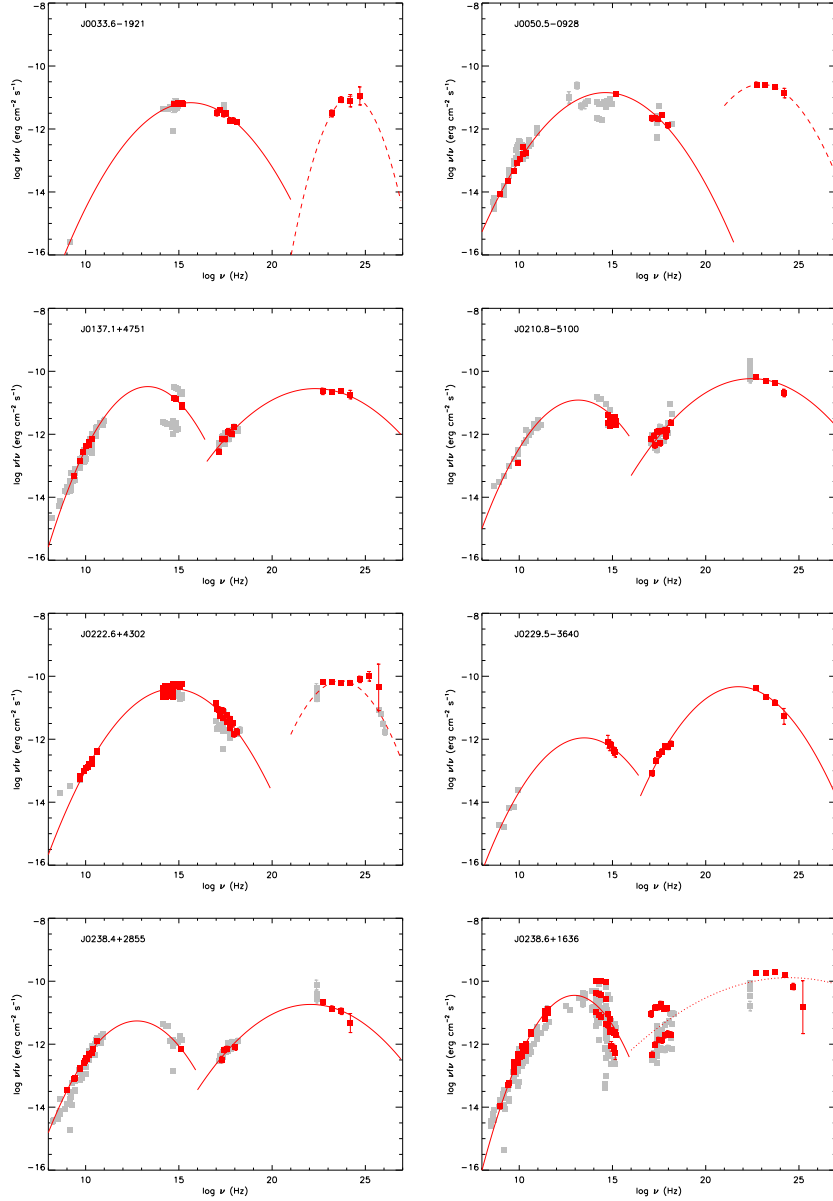


Fig. 6.— The red points for the quasi-simultaneous data, while the grey ones represent other observations (see, Abdo et al. 2010b, for detail description). Both SEDs of synchrotron and IC components are fitted by a log-parabolic law, i.e., $\log \nu f_\nu = -b(\log \nu - \log \nu_p)^2 + \log \nu_p f_\nu^p$. The IC component of 14 out of 48 blazars covers only γ -ray band (see Table 1 for name list), and the IC curvature of J1719.3+1746 and 2202.4+4217 are obviously smaller than that of other blazars. These 16 IC fitting curves are shown as red dashed lines. For J0238.6+1636, J0538.8-4403, J2254.0+1609, and J2345.5-1559, the IC fittings significantly depart from the observational SED, especially inconsistent with the γ -ray spectral index. These 4 IC fitting curves are presented as red dotted lines. All fitting parameters are presented in Table 1. See context for detail.

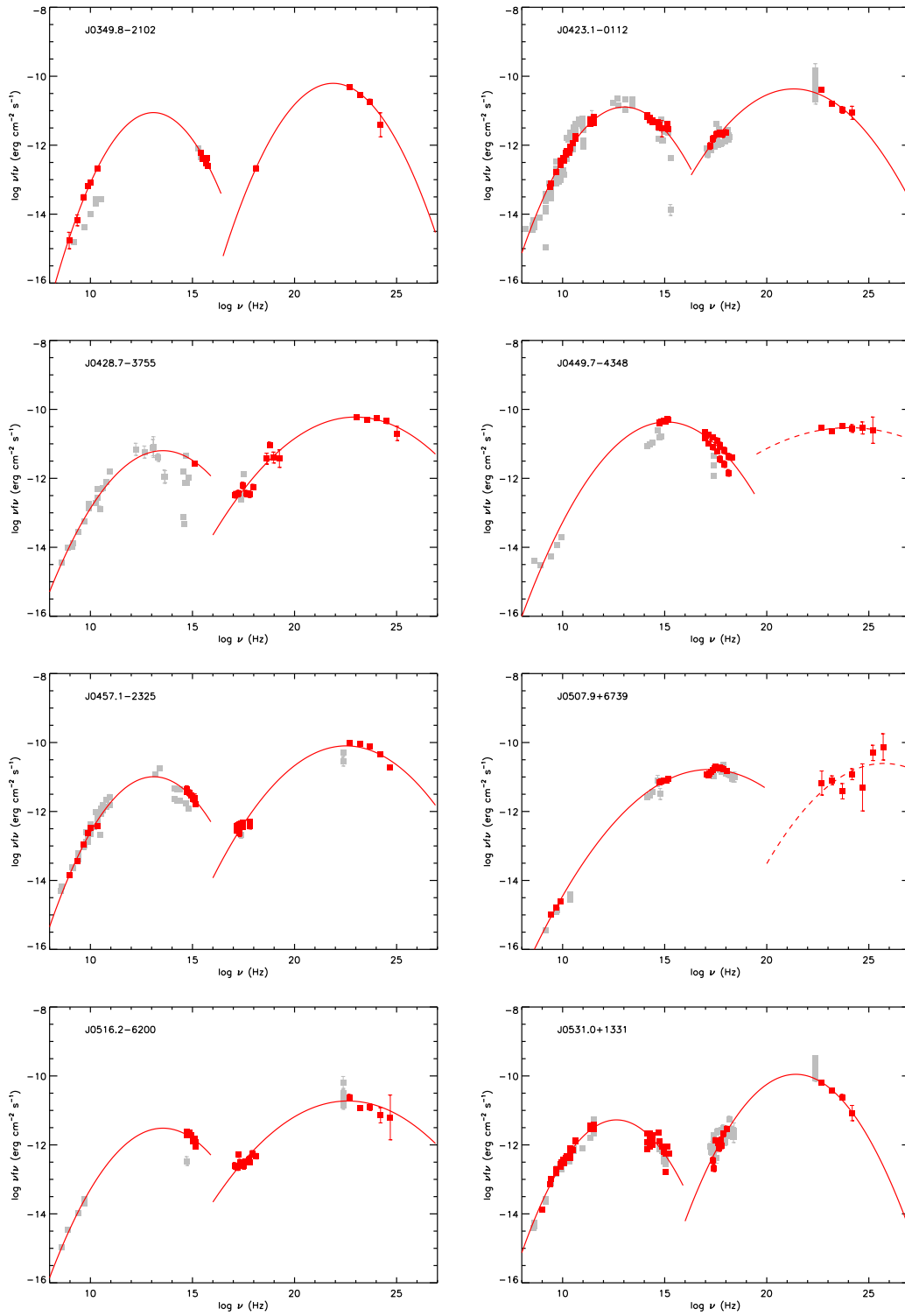


Fig. 6 — continued.

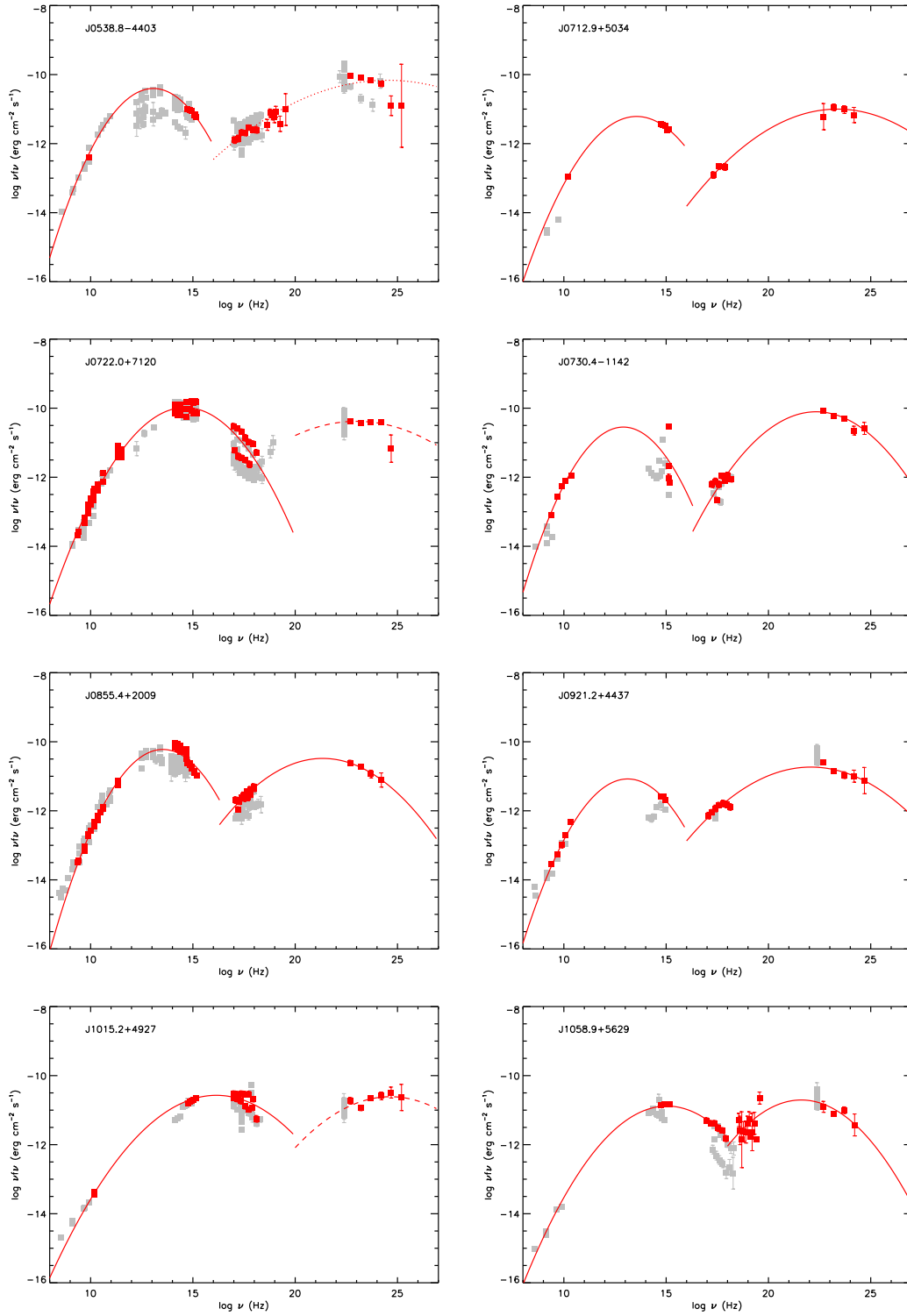


Fig. 6 — continued.

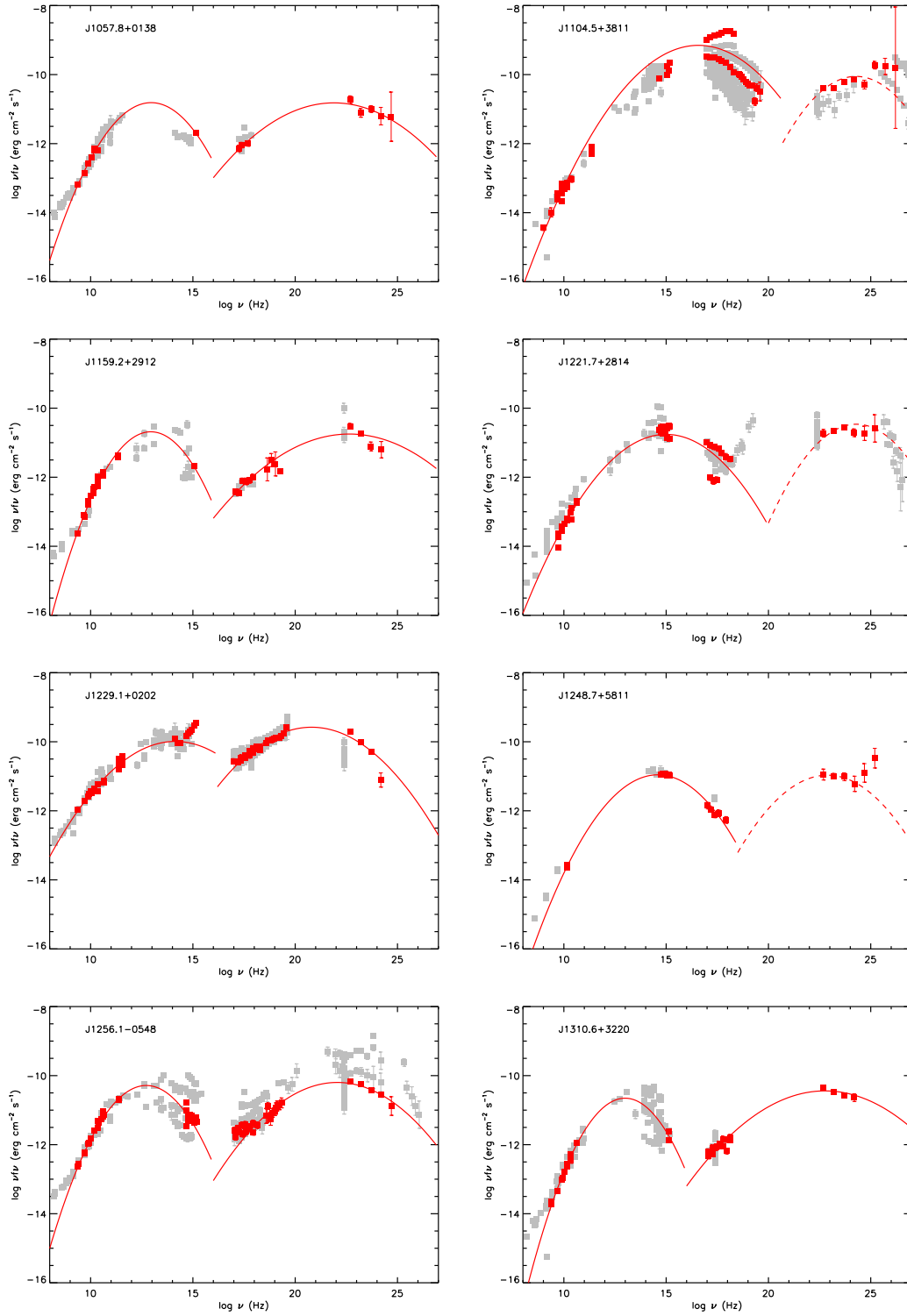


Fig. 6 — continued

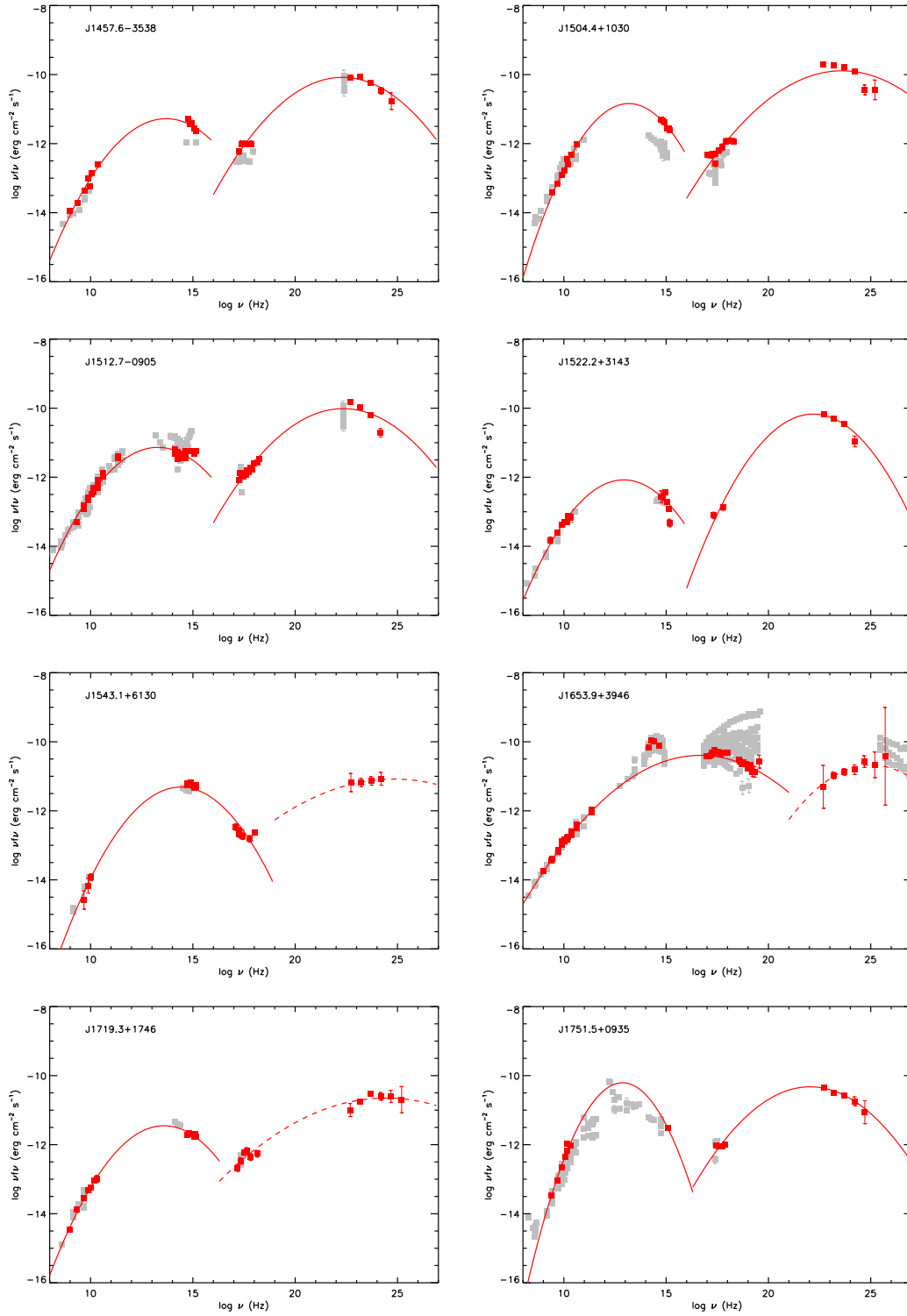


Fig. 6 — continued.

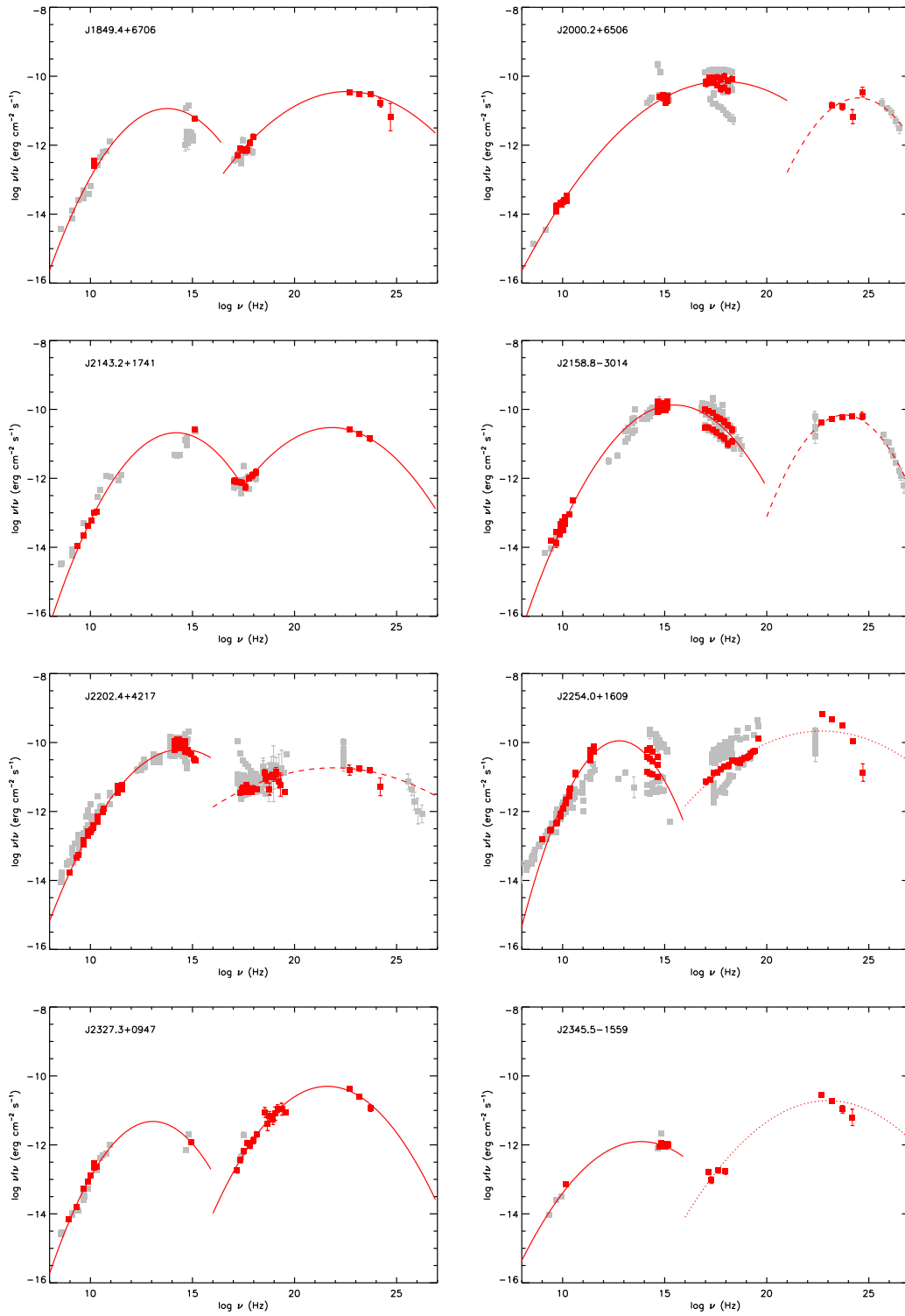


Fig. 6 — continued.

A. Figures

B. compare with empirical relation/correlation

Abdo et al. (2010b) presented an empirical relation between radio flux density, synchrotron peak frequency, and synchrotron peak flux, i.e., $\log \nu_p f_{\nu_p} = 0.5 \log \nu_p - 20.4 + 0.9 \log(R_{5\text{GHz}})$, where $R_{5\text{GHz}}$ is the radio flux density at 5 GHz in units of mJy, ν_p the synchrotron peak frequency in unit of Hz, and $\nu_p f_{\nu_p}$ the synchrotron peak flux in unit of $\text{erg s}^{-1} \text{cm}^{-2}$ (Equation 4 in Abdo et al. 2010b). A similar relation can be derived by combining a log-parabolic law of SED ($\log \nu f_\nu = -b(\log \nu - \log \nu_p)^2 + \log \nu_p f_{\nu_p}$) and the correlation between peak frequency and curvature ($1/b = A + B \log \nu_p$),

$$\log \nu_p f_{\nu_p} = \log \nu f_\nu + \frac{(\log \nu - \log \nu_p)^2}{A + B \log \nu_p}. \quad (\text{B1})$$

The comparison of these two relations is shown in Figure 7, where the blue dots are synchrotron peak fluxes calculated by two relations from Mote-Carlo simulation by randomizing the values of synchrotron peak frequency and 5 GHz flux density. The red line is the perfect one-to-one relation. We can see that these two relations are roughly consistent with each other.

As early in 1990s people found an empirical correlation between the synchrotron peak frequency and the radio to optical broadband spectral index (see e.g., Padovani & Giommi 1995; Fossati et al. 1998; Padovani et al. 2003). A similar relation can also be derived when combining $\log \nu f_\nu = -b(\log \nu - \log \nu_p)^2 + \log \nu_p f_{\nu_p}$ and $1/b_{sy} = A + B \log \nu_p$. If f_{ν_1} and f_{ν_2} are flux densities at ν_1 and ν_2 , respectively, one has,

$$\begin{cases} \log \nu_1 f_{\nu_1} = -b(\log \nu_1 - \log \nu_p)^2 + \log \nu_p f_{\nu_p} \\ \log \nu_2 f_{\nu_2} = -b(\log \nu_2 - \log \nu_p)^2 + \log \nu_p f_{\nu_p}. \end{cases} \quad (\text{B2})$$

Substituting the relation $1/b_{sy} = A + B \log \nu_p$ and a broadband spectral index $\alpha_{12} = -(\log f_{\nu_2} - \log f_{\nu_1}) / (\log \nu_2 - \log \nu_1)$ into the Equation B2, one gets,

$$\log \nu_p = \frac{A(1 - \alpha_{12}) + (\log \nu_2 + \log \nu_1)}{2 - B(1 - \alpha_{12})}. \quad (\text{B3})$$

This preprint was prepared with the AAS L^AT_EX macros v5.2.

²Note that relation $1/b_{sy} = A + B \log \nu_p$ is derived in AGN frame. While this relation is assumed to be valid in the observational frame, because the uncertainty caused by transformation from AGN to observational frames (i.e., $\nu_p^{obs} = \nu_p / (1 + z)$) is smaller than the scatter of the correlation. Similar for following analysis.

The Figure 8 indicates the correlation between the synchrotron peak frequency and the radio to optical broadband spectral index, where the blue squares and the black open dots are data collected from Fossati et al. (1998) and Padovani et al. (2003), respectively. The red solid line is derived from Equation B3, and the red dashed lines indicate the 3σ confidence bands. The radio frequency and optical wavelength are taken at 5 GHz and 5100 Å, which are same as those in Fossati et al. (1998) and Padovani et al. (2003). We can see that even though the data are systemically higher than the theory around $\nu \sim 10^{14}$ Hz, the trend of the data generally agrees with theory.

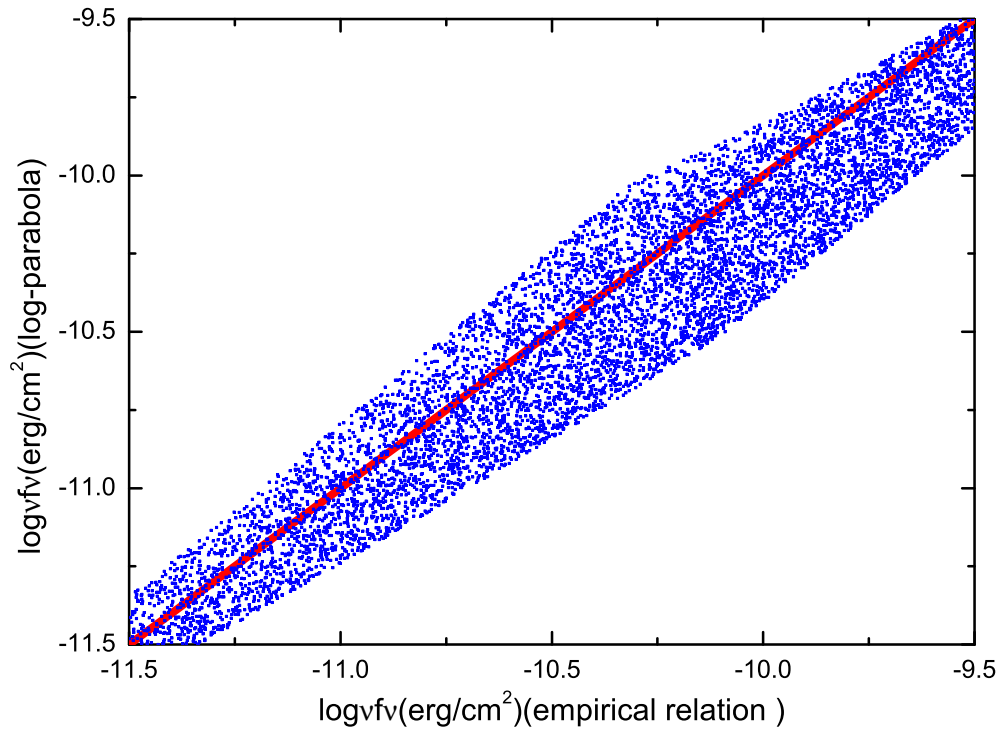


Fig. 7.— Comparison between the synchrotron peak fluxes derived from empirical relation (Abdo et al. 2010b) and that derived from Equation B1. The blue dots are from Monte-Carlo simulation by randomizing values of synchrotron peak frequency and 5 GHz flux density. The red line is the perfect one-to-one relation. See context for detail.

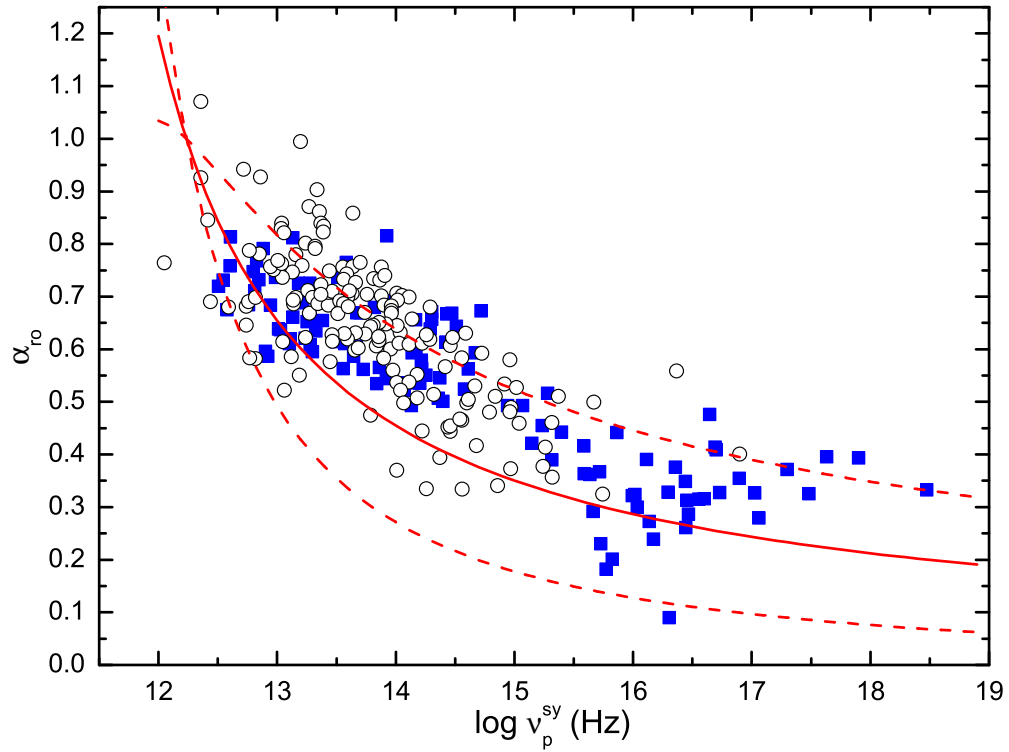


Fig. 8.— Broadband spectral indexes α_{ro} versus synchrotron peak frequency. Blue squares and open dots are data taken from Fossati et al. (1998) and Padovani et al. (2003), respectively. The red solid line is derived from Equation B3, the red dashed lines indicate the 3σ confidence bands. The radio frequency and optical wavelength are selected at 5 GHz and 5100 Å, which are same as in these samples.